―研究論文―
Scientific Paper

Layered conductance in the ionosphere estimated using data from a multi-wavelength photometer at the European Incoherent Scatter radar site

Shin-ichiro Oyama[1*], Taiki Watanabe[1, 3], Ryoichi Fujii[1],
Satonori Nozawa[1] and Takuo T. Tsuda[2]

欧州非干渉散乱（EISCAT）レーダー観測所の多波長フォトメータデータを用いた
層状電離圏電導度の推定

大山伸一郎 [1*]・渡邉太基 [1, 3]・藤井良一 [1]・野澤悟徳 [1]・津田卓雄 [2]

要旨:　本研究では，多波長フォトメータデータ（427.8 nm, 557.7 nm, 630.0 nm）を利用してオーロラ発生時の高緯度電離圏における電気伝導度推定の手法開発を行った．本手法の特徴は層状の電気伝導度を導出することが可能な点である．この層構造を持つ電気伝導度を光学データから導出するためのモデル関数を，高度分解能がある欧州非干渉散乱（EISCAT）UHF レーダーデータから推定した電気伝導度を用いて決定した．本研究により，電離圏を3層（高度 95–110 km, 110–170 km, 170–300 km）に分割しても，従来の方法と同程度の信頼度を持つ電気伝導度を光学データから導出できることが確認された．

Abstract:　This study aimed to develop a methodology for estimating ionospheric conductance at auroral latitudes using data from a multi-wavelength photometer (427.8, 557.7, and 630.0 nm). An advantage of the approach is that the ionosphere is divided into layers and conductance is computed for each layer. From optical data, the layer conductance was determined by using height-resolved conductivity derived from the European Incoherent Scatter (EISCAT) Tromsø UHF radar. The developed method can provide conductance from optical data with some confidence (at least at the same level as previous methods) even after separating the ionosphere into three layers, 95–110 km, 110–170 km, and 170–300 km.

1.　Introduction

　　The study of ionospheric conductance has a long history, with pioneering researchers pointing out the importance of the magnetosphere-ionosphere current system more than a

[1]　名古屋大学太陽地球環境研究所．Solar-Terrestrial Environment Laboratory, Nagoya University, Furo-cho, Chikusa-ku, Nagoya 464-8601.

[2]　情報・システム研究機構国立極地研究所．National Institute of Polar Research, Research Organization of Information and Systems, Midori-cho 10–3, Tachikawa, Tokyo 190-8518.

[3]　（現所属 present affiliation）: 株式会社タマディック．TAMADIC Co., Ltd., Oechou 6–19, Ryoukou Bld. Minami-kan 5-kai, Minato-ku, Nagoya 455-0024.

[*]　Corresponding author. E-mail: soyama@stelab.nagoya-u.ac.jp

hundred years ago (Schuster and Lamb, 1889; Schuster, 1908). The methodology for estimating the ionospheric conductance, especially at high latitudes, has also been long discussed. The conductance associated with auroras tends to have complicated horizontal patterns with greater temporal variations than occur at middle and low latitudes. Optical instruments such as the all-sky camera are useful diagnostic tools for capturing such variable structures on a time scale of seconds. Furthermore, some relationships are known to exist between auroral emission intensity and ionospheric conductance (Campbell and Leinbach, 1961; Ansari, 1964). However, further studies are required to improve understanding of these relationships.

Many researchers have tried to develop model functions that can reproduce the conductance from optical measurements. One modeling approach applies data from the incoherent scatter (IS) radar (Mende *et al*., 1984; Kosch *et al*., 1998, 2001). IS radar can provide height-resolved conductivity, which is used for calculating the height-integrated conductivity or conductance (Brekke *et al*., 1974; Banks *et al*., 1981; Vickrey *et al*., 1981, 1982; Robinson and Vondrak, 1984; Vondrak and Robinson, 1985; Robinson *et al*., 1985, 1987; Brekke and Hall, 1988; Robinson *et al*., 1989; Senior, 1991; Moen and Brekke, 1993; Senior *et al*., 2007). The model function may be determined by comparison with optical data. For example, Mende *et al*. (1984) and Kosch *et al*. (1998) suggested that the Pedersen conductance, but not the Hall conductance, can be reasonably estimated from optical data. Some studies have suggested that the cosmic radio noise absorption measured with a riometer provides a more reasonable estimation for the Hall conductance than application of optical data because the Hall conductivity tends to peak at lower heights (sometimes in the D region) than the typical aurora emission layers (Walker and Bhatnagar, 1989; Senior *et al*., 2007).

The aim of the present study was to develop a method for estimating conductance from optical data. Auroral emission intensities measured with a photometer at three wavelengths (427.8, 557.7, and 630.0 nm) are analyzed to estimate the conductance in several layers (hereafter referred to as layered conductance). Height-resolved conductivity estimated using data from the European Incoherent Scatter (EISCAT) UHF radar at Tromsø, Norway, is compared with auroral emission intensity. A notable advantage of the dataset used in this study is that both the photometer and EISCAT UHF radar were fixed along the magnetic field line. The theoretical approach for estimation of the layered conductance is described in Section 2. Section 3 discusses the instruments and datasets analyzed in this paper. Section 4 presents the relationship between the conductance derived from EISCAT radar data and that from photometer data. Section 5 assesses the validity of the developed model function and also presents the magnetic local time (MLT) dependence of the model function. As an example, the model function is applied to a two dimensional image taken with an all-sky camera at the Tromsø radar site. The results of the study are summarized in Section 6.

2.   Theoretical approach

Ionospheric conductivity is one of the fundamental and important parameters in the magnetosphere-ionosphere-thermosphere coupled system. Since the theoretical equation and its application to IS-radar data have been well established by many researchers (*e.g.*,

Brekke and Moen, 1993), these are not iterated in this paper. A theoretical relationship between conductance and auroral emission intensity has also been described by Kosch *et al.* (1998). However, this theoretical relationship is described here because it was modified for estimating layered conductance from optical data.

A key parameter for understanding this relationship is the ion production rate due to auroral particle precipitation. The production rate is a function of electron density and, to the first order, is proportional to the emission intensity (Kosch *et al.*, 1998). Solar radiation is also an important source of ionization, but it is ignored here because our focus is on ionization during the dark night. In this paper, we assume a steady state condition, which requires smaller divergence associated with the electron flux than does the time derivative term in the continuity equation (Kosch *et al.*, 2001). This assumption allows us to express the production rate (Q_p) in the E region (below 170 km) as follows (Vondrak and Baron, 1976; Wallis and Budzinski, 1981; Robinson and Vondrak, 1984; Rasmussen and Schunk, 1988; Kosch *et al.*, 1998):

$$Q_p = \alpha N_e^2, \tag{1}$$

where N_e is the electron density and α is the effective recombination coefficient (Vickrey *et al.*, 1982). Above 170 km, or in the F region, the lifetime of ionized particles is long enough that the transport process becomes important. In this case the production rate can be written using the coefficient β as follows:

$$Q_p = \beta N_e. \tag{2}$$

Since the emission intensity (I) is proportional to the production rate (Kosch *et al.*, 1998) and the conductance (Σ) is proportional to the electron density (Brekke and Moen, 1993), we can obtain the following relationships:

$$\Sigma \propto \sqrt{I} \qquad \text{below 170 km} \tag{3 a}$$

$$\Sigma \propto I \qquad \text{above 170 km.} \tag{3 b}$$

Since there is no auroral emission line that always covers the height of the entire ionosphere, it is reasonable to separate the ionosphere into several layers when estimating conductance from optical data. For example, the emission lines at 427.8 nm and 557.7 nm can be representative of the E region and that at 630.0 nm of the F region. In this case, the conductance can be written as the summation of the conductances estimated by individual emission lines:

$$\Sigma = (\alpha_{427.8}\sqrt{I_{427.8}} + \gamma_{427.8}) + (\alpha_{557.7}\sqrt{I_{557.7}} + \gamma_{557.7}) + (\beta_{630.0} I_{630.0} + \gamma_{630.0}). \tag{4}$$

A comparison between the EISCAT-derived and optically derived conductances can provide the coefficients α_λ, β_λ, and γ_λ by applying the least mean-square method to *eq.* (4). As a first step, the emission layers at 427.8 nm, 557.7 nm, and 630.0 nm are assumed to be distributed mainly from 95 to 110 km, 110 to 170 km, and 170 to 300 km, respectively. However, the heights of the emission layers may vary with the precipitation energy of the auroral particles, so some different height regions are also tested in the calculation to determine the

dependencies on emission height. The quenching process plays an important role in auroral/ airglow emission. However, this effect is not considered here because a theoretical calculation including the quenching process by molecular oxygen and nitrogen at a height of around 230 km gives a lifetime of the excited $O(^1D)$ of about 30 s (Gustavsson *et al*., 2000), which is shorter than the integration time adopted for the EISCAT and photometer data in this study. Furthermore, a model calculation of the 630 nm intensity using EISCAT radar data (60 s integration time) showed good correlation with the photometer measurement (Oyama *et al*., 2000).

3. Instrumentation and datasets

The multi-wavelength photometer at the Tromsø EISCAT radar site is fixed to look along the magnetic field line with a view angle of about 1.2°. The airglow and auroral light is divided into three photomultipliers, which have individual optical filters. The photometer has been operated during dark winter nights since 2001. Measurements with the 557.7 nm optical filter have been made since October 2004. In this paper, data obtained in October and December 2006 (listed up in Table 1) are analyzed. The data sampling rate is 20 Hz, and a 60 s average is used in this paper. Before and after the observation seasons (generally September and April), the photometer is calibrated at the National Institute of Polar Research, Japan, to estimate variations in the characteristics of the optical filter and the photomultiplier. The weather conditions are checked by using sky images taken with a digital camera, which is located in the same optical hut.

Simultaneous data from the photometer and the EISCAT UHF radar are used for the present analysis. Furthermore, field-aligned data from the EISCAT radar must be chosen in order to synchronize the measurement volume with the photometer. The EISCAT data are also averaged for 60 s, in accordance with the photometer data analysis. To estimate the conductivity, equations published by Brekke and Hall (1988) are applied to the EISCAT data.

4. Results

The theoretical approach mentioned in Section 2 indicates that the electron density below an altitude of 170 km is proportional to the square root of the emission intensity and

Table 1.   Datasets analyzed in this paper.

Start time (UT)		End time (UT)	
04 - Oct - 2006	21 : 00	04 - Oct - 2006	23 : 59
05 - Oct - 2006	19 : 18	05 - Oct - 2006	23 : 00
18 - Oct - 2006	18 : 12	18 - Oct - 2006	23 : 59
19 - Oct - 2006	00 : 26	19 - Oct - 2006	00 : 59
19 - Oct - 2006	18 : 08	19 - Oct - 2006	23 : 59
20 - Oct - 2006	18 : 04	20 - Oct - 2006	19 : 58
15 - Dec - 2006	00 : 01	15 - Dec - 2006	05 : 21

that above 170 km it is linearly proportional to it. The conductivity has the same proportionality as does the electron density. The representative wavelengths of auroral emission below 170 km are 427.8 nm and 557.7 nm. The peak in the emission layer of the 427.8 nm wavelength tends to have a peak at lower height than that of the 557.7 nm wavelength. As the first step in the calculation, we assume that the main parts of the emissions of the 427.8 nm and 557.7 nm wavelengths are located between 95 and 110 km and between 110 and 170 km, respectively. In this paper, these two layers are referred to as the lower and upper E regions, respectively. The conductance in the F region is integrated between 170 and 300 km, and the representative emission wavelength is 630.0 nm.

Figures 1 a, b, and c show the relationship between the Pedersen conductances calculated using data from the EISCAT UHF radar (hereafter referred to as EISCAT conductance) and the emission intensity measured with the photometer. The number of measurements used in this study is about 1700. Following the theoretical prediction, the F region conductance (Fig. 1 a) is fitted with a linear function, and the upper and lower E region conductances (Figs. 1 b and c, respectively) are fitted by the square roots of the emission intensities at 557.7 and 427.8 nm, respectively. The same fitting procedure is applied to the Hall conductance, as shown in Fig. 2. The coefficients of α_λ, β_λ, and γ_λ in *eq.* (4) can be derived by the least mean-square method, and the results are summarized in Table 2. Table 2 also presents the 95 % confidence of each coefficient. This value can be used to calculate the estimation error through the fitting procedure, and the error is on the order of 1 %. However, the gross error, including effects of ambiguity of the observed data, may be greater than 1 % according to the mean difference in Table 3, which will be presented later. A data group in Fig. 1 c has a different trend from the other measurements, but the reason for this difference is unclear.

Figures 1 and 2 suggest that the three emission intensities appear to be appropriate indicators for estimating the layered conductance. To quantitatively describe the fitted curve, we calculated the R-square value. We then calculated the conductance by using the photometer data (hereafter referred to as photometer conductance) and made statistical comparisons. Table 3 shows the R-square between the EISCAT and photometer conductances. Table 3 also shows the mean difference between the two conductances. This value can be regarded as the gross error made through the estimation procedure and the ambiguity of the observed data. Although the mean difference is dependent on the layer, it is less than 2.3 S (for the case of Σ_H in the lower E region). However, it is not meaningful to discuss the mean difference itself because the ratio of the mean difference to the conductance is more important. In the case of the Pedersen conductance, the layered conductances in the lower and upper E regions and in the F region have values up to approximately 2, 30, and 3 S, respectively (see Fig. 1). Thus, the Pedersen component distributes mainly in the upper E region (from 110 to 170 km). A comparison of the layered Pedersen conductance with the mean difference suggests that the fitting procedure works well for the upper E region and the F region cases but that it does work as well for the lower E region. On the other hand, the layered Hall conductances have values up to approximately 30, 20, and less than 0.1, respectively (see Fig. 2). The Hall conductivity distributes in the lower and upper E region (from 95 to 170 km) and has no significant values in the F region. The layered Hall conductance (except for the F region) appears to be reproduced better than the Pedersen conductance. The statistical results shown in Table 3 suggest that both layered

Pedersen conductance
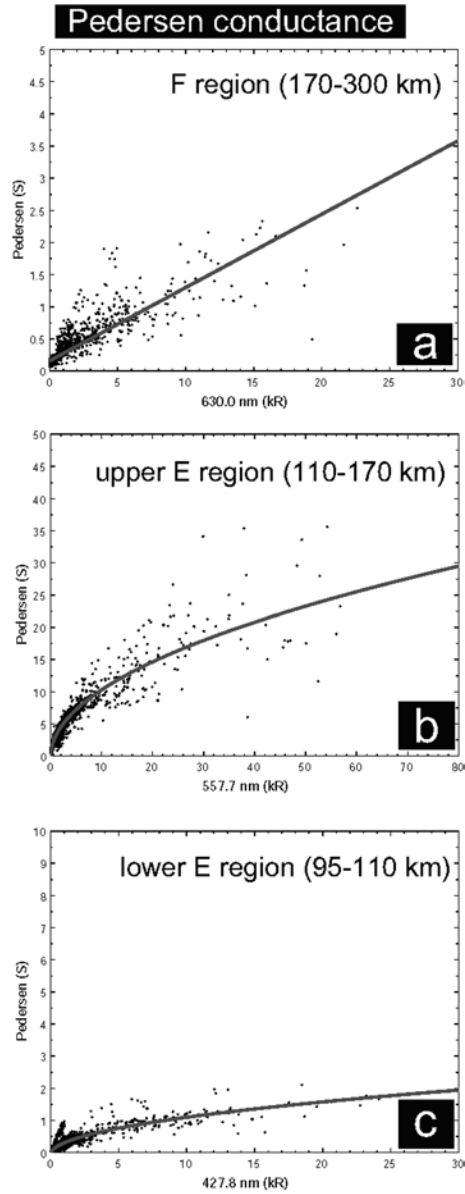
Fig. 1. *Relationship between emission intensity (a: 630.0 nm, b: 557.7 nm, c: 427.8 nm) and the height-integrated Pedersen conductivity, or conductance, calculated using the EISCAT radar data in (a) the* F *region (170–300 km), (b) the upper* E *region (110–170 km), and (c) the lower* E *region (95–110 km). The best-fitted function is shown by the gray curve.*
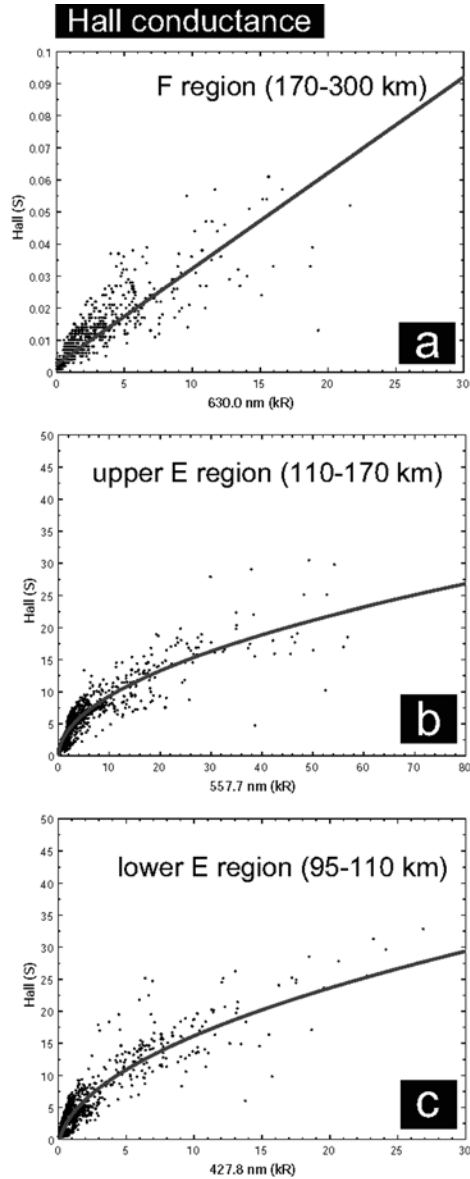
Fig. 2.   Same as Fig. 1 but for the Hall conductance.

conductances can be reproduced well by the fitting procedure using the three wavelengths.

The major layer for each component may be presented more clearly by calculating the ratio of the layered conductance to the whole conductance. Figure 3 shows the ratio for (a) the Pedersen conductance and (b) the Hall conductance. The occurrence rate is normalized by the maximum at each layer. In the case of the Pedersen conductance, more than 80 % of the entire conductance is generally in the upper E region (110−170 km), which is consistent

Table 2.   Coefficients of the best-fitted function to reproduce the layered conductance from the photometer data shown in Figs. 1 and 2. The layers are defined as 95–110 km for the lower E region, 110–170 km for the upper E region, and 170–300 km for the F region.

Layer		α or β		γ	
		value	95% confidence	value	95% confidence
Σ_P	F	1.1×10^{-4}	3.1×10^{-6}	1.6×10^{-1}	8.3×10^{-3}
	Upper E	1.1×10^{-1}	1.7×10^{-3}	-2.1×10^{-1}	1.0×10^{-1}
	Lower E	1.2×10^{-2}	3.3×10^{-4}	-6.1×10^{-2}	1.2×10^{-2}
Σ_H	F	3.0×10^{-6}	7.1×10^{-8}	2.4×10^{-3}	1.9×10^{-4}
	Upper E	9.6×10^{-2}	1.6×10^{-3}	-2.9×10^{-1}	9.7×10^{-2}
	Lower E	1.8×10^{-1}	3.6×10^{-3}	-1.9	1.3×10^{-1}

Table 3.   R-square value and mean difference between the EISCAT and photometer conductances in the lower and upper E regions and in the F region. The three-wavelength method was employed to make this table.

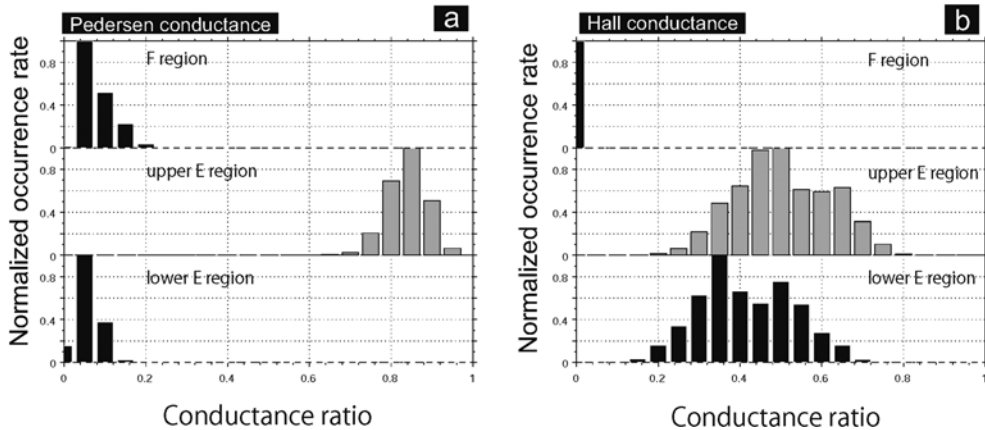|	Σ_P		Σ_H	
	R-square	mean difference	R-square	mean difference
F region	0.75	0.09	0.79	0.002
upper E region	0.89	0.9	0.88	2.2
lower E region	0.73	1.3	0.85	2.3

Fig. 3.   Occurrence rate of the ratio of the layered conductance to the whole conductance in the lower and upper E regions and the F region (from bottom to top) for (a) the Pedersen conductance and (b) the Hall conductance. The bin width of the ratio is 0.05, and the occurrence rate is normalized by the maximum value in each layer.

with the statistical peak of 120 km (Schlegel, 1988; Senior, 1991). The lower E region and the F region are minor parts (less than 20 %) of the Pedersen conductance. This result is consistent with previous results (Vickrey *et al.*, 1981; Brekke and Hall, 1988; Rasmussen and Schunk, 1988). Notably, the F region conductance is comparable with the lower E region conductance. In the case of the Hall conductance, the E region value is the major component and the F region one is often negligible. Although the peak occurrence rate appears at a slightly higher conductance ratio for the upper E region than for the lower E region, the histogram shape is similar for both cases. Although the upper E region conductance is slightly larger than the lower E region conductance, these two layers make almost the same contribution to the entire Hall conductance.

5.   Discussion

5.1.   Validity of the method
5.1.1.   Comparison with other methods

In the previous section, photometer data taken at the three wavelengths were applied to estimate the layered conductance. However, some previous studies have proposed a methodology using only one wavelength, such as 557.7 nm, to reproduce the conductance integrated from the E region to the F region. In this section, we compare the three-wavelength method with the one-wavelength method. Figure 4 shows (a) the Pedersen and (b) the Hall components of the photometer and EISCAT conductances. Values derived by the three-wavelength and one-wavelength methods are shown with black and red dots, respectively. Both 557.7 nm and 427.8 nm data were tested for the one-wavelength method, and the figure presents results for the 557.7 nm case. Values of the layered conductance
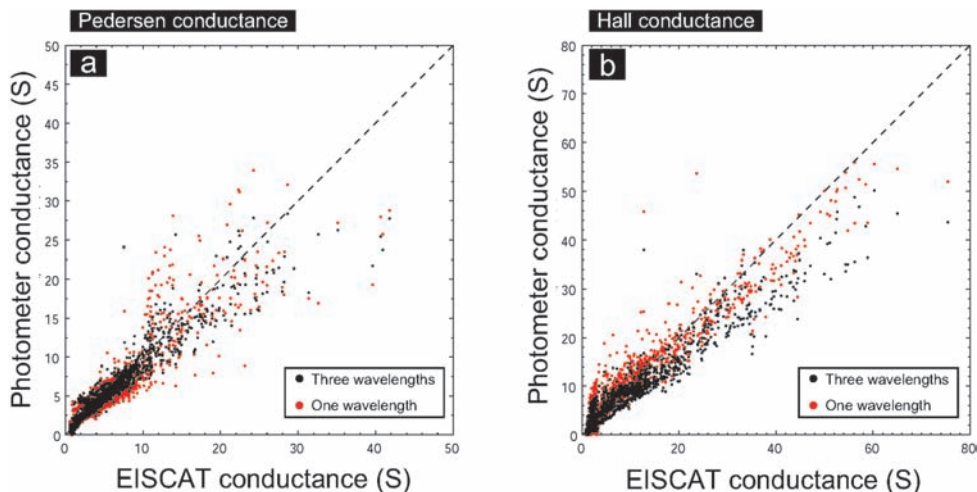

Fig. 4.   Relationships between the EISCAT and photometer conductances for (a) the Pedersen conductance and (b) the Hall conductance derived with the one-wavelength method (red dots) and the three-wavelength method (black dots). Values for the one-wavelength method are from photometer data at 557.7 nm.

Table 4.   Same as Table 3 but for the whole conductance. The one-wavelength (1λ) and the three-wavelength (3λ) methods are compared in the table.

Σ_P						Σ_H					
R-square			mean difference			R-square			mean difference		
1 λ		3 λ	1 λ		3 λ	1 λ		3 λ	1 λ		3 λ
427.8	557.7		427.8	557.7		427.8	557.7		427.8	557.7	
0.82	0.9	0.91	1.4	0.9	0.83	0.89	0.9	0.92	2.3	2.2	2.2

Table 5.   Comparison of the R-square and mean difference between one- and two-wavelength methods.

Σ_P							
R-square				mean difference			
2 λ		1 λ		2 λ		1 λ	
427.8 +630.0	557.7 +630.0	427.8	557.7	427.8 +630.0	557.7 +630.0	427.8	557.7
0.83	0.91	0.82	0.90	1.4	0.8	1.4	0.9
Σ_H							
R-square				mean difference			
2 λ		1 λ		2 λ		1 λ	
427.8 +630.0	557.7 +630.0	427.8	557.7	427.8 +630.0	557.7 +630.0	427.8	557.7
0.89	0.90	0.89	0.90	2.3	2.3	2.3	2.2

from the three-wavelength method were summed to create the figure.

As expected, the photometer conductances derived from both methods agree well with the EISCAT conductance. Table 4 presents the R-square and mean difference values. Values obtained by using 427.8 nm instead of 557.7 nm were also tabulated for the one-wavelength method. There are no notably large differences among the three methods in each index, but the 557.7 nm and three-wavelength cases appear to have slightly better goodness of fit than the 427.8 nm case. Most importantly is that all three methods show approximately the same prediction performance.

Table 5 presents statistical results for the one- and two-wavelength methods. The two-wavelength method employs one of the *E* region emission lines (427.8 nm or 557.7 nm) to reproduce the conductance from 95 to 170 km and uses 630.0 nm for the *F* region conductance (170−300 km). The R-square and mean difference for the two-wavelength method do not notably differ from those for the one-wavelength method, but the values using 427.8 nm data appear to be worse than those using 557.7 nm data. This result may be related to the 427.8 nm emission layer being narrower than the 557.7 nm layer.

In this section, three types of methods have been applied for estimating the photometer conductance. No notable differences were found among the methods, suggesting that the three-wavelength method developed in this study does not dramatically improve previous methods of conductance estimation from optical data. The three-wavelength method can reproduce the layered conductance at the same level of accuracy as the one-wavelength

Table 6.   R-square and mean difference between the EISCAT and photometer conductances in the lower and upper E *regions with changing border altitude between the two regions. The three-wavelength method was employed to derive the photometer conductance.*

Border altitude (km)	Layer	Σ_P		Σ_H	
		R-square	mean difference	R-square	mean difference
105	Lower E region	0.88	0.1	0.87	1.0
	Upper E region	0.90	0.8	0.90	1.4
110	Lower E region	0.73	0.1	0.85	1.3
	Upper E region	0.89	0.7	0.88	0.8
120	Lower E region	0.86	0.4	0.89	2.0
	Upper E region	0.88	0.6	0.89	0.3

method. This is a notable advantage and one of the main objectives of this study, as mentioned in Section 1.

5.1.2.   Significance of the altitude of the border between the lower and upper E regions

The layered conductance results mentioned in Section 5.1.1. were obtained by employing a fixed border altitude between the lower and upper E regions, *i.e.*, 110 km. However, the fixed border altitude could cause some estimation errors because the 427.8 nm and 557.7 nm emission heights can vary depending on auroral particle energy. Table 6 shows the statistical values derived by choosing two different border altitudes, 105 km and 120 km, along with the values for the case of 110 km as a reference. Although the R-square for the lower E region case at the border altitude of 110 km may be slightly smaller than for the other cases, no significant differences were identified. We also tested other border altitudes, but again no notable differences appeared. The results in the table suggest that the derivation of photometer conductance does not strongly depend on the definition of the border altitude.

Coefficients of the model equation for representing photometer conductance at each layer are summarized in Tables A1 and A2 in Appendix A. These coefficients may be useful for future work involving the estimation of layered conductance using optical data. The coefficient α for the lower E region conductance increases with increasing border altitude; by contrast, that for the upper E region conductance decreases. This occurs because of the change in the integrated altitude range.

In Section 5.1., the three-wavelength method was evaluated by seven methods. The major difference between the methods is the combination of the 557.7 nm and 427.8 nm wavelengths. However, independent of the combination, all of the methods provide good agreements with the EISCAT conductance. The good agreement suggests that one of the E region emissions can represent the other even if the chosen emission layer does not cover the entire range from 95 to 170 km altitude. In other words, the number flux spectrum of auroral particles does not have notable peaks in the energy range corresponding to the 427.8 nm and 557.7 nm emission layers, and the variation in the 427.8 nm (557.7 nm) intensity is proportional to that for 557.7 nm (427.8 nm). Figure 5 shows the mean spectrum of the number flux derived using the CARD method (Brekke *et al*., 1989; Fujii *et al*., 1995). Figure 5 is made from the EISCAT radar data (same dataset used for the conductance
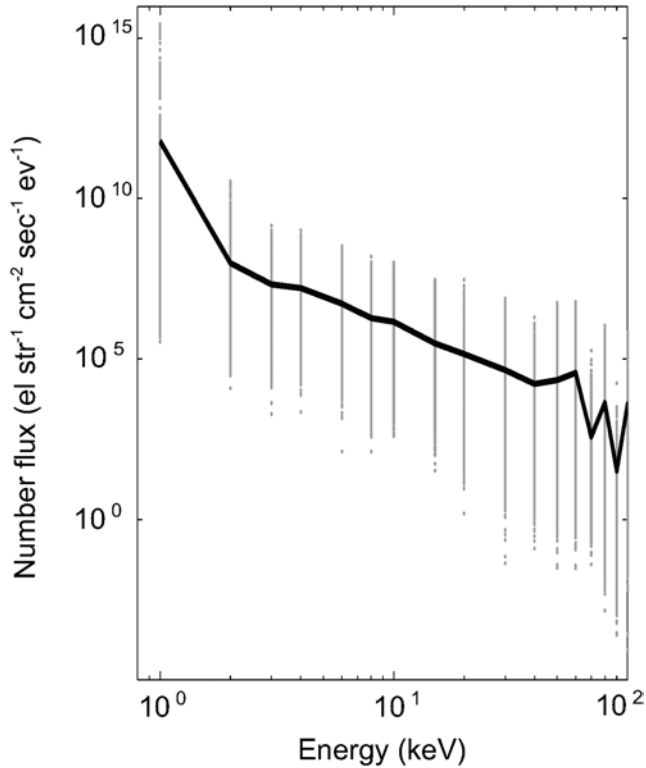
Fig. 5. Mean spectrum of the energy flux of the precipitated electrons. The spectrum was estimated with the CARD method by applying EISCAT data taken simultaneously with the photometer data.

calculation). Spectra were obtained every 1 min from the height profile of the EISCAT electron density, and approximately 1700 spectra were averaged to make the figure. All spectra are plotted by gray dots, and the mean spectrum is plotted by a black curve. The mean spectrum decreases approximately linearly in a logarithmic scale between 2 and 40 keV. Since this energy range represents a major contributor to auroral emission at 427.8 nm and 557.7 nm, these emission intensities can be synchronized. This result is consistent with the finding that there is no significant difference between the methods for estimating photometer conductance.

5.2. MLT dependence of the best-fitted coefficients

Some previous studies using data from satellites and IS radars have addressed the MLT dependencies of the particle precipitation energy (Wallis and Budzinski, 1981; Vickrey *et al.*, 1982; Ahn *et al.*, 1983; Hardy and Gussenhoven, 1985): harder particle precipitation in the post-midnight period than in the pre-midnight period. Harder particle precipitation ionizes neutral particles at lower altitudes, which enhances conductivity in the lower *E* region or possibly in the *D* region. However, this is the case only for the Hall conductivity, not for the Pedersen conductivity, because the Hall conductivity can have a peak of the

Table 7. (a) Coefficients of the best-fitted function to reproduce the layered Pedersen conductance from the photometer data. The border altitude between the lower and upper E regions is 110 km. The three-wavelength method was applied to make the table. The dataset is classified by two time intervals: magnetic pre-midnight, or evening, and magnetic post-midnight, or morning (the magnetic midnight at Tromsø is 2030 UT). The ratio of α is also tabulated to determine the difference between the two time intervals. (b) Same as Table 7a but for the Hall conductance.

(a)

MLT	Layer	α or β value	α or β 95% confidence	γ value	γ 95% confidence
Evening	Lower E	9.8×10^{-3}	1.3×10^{-3}	-8.7×10^{-3}	3.2×10^{-2}
	Upper E	1.0×10^{-1}	2.6×10^{-3}	-1.8×10^{-1}	1.1×10^{-1}
	F	2.7×10^{-4}	1.1×10^{-5}	9.4×10^{-2}	1.1×10^{-2}
Morning	Lower E	1.2×10^{-2}	3.2×10^{-4}	-8.0×10^{-2}	1.4×10^{-2}
	Upper E	1.1×10^{-1}	2.4×10^{-3}	-1.5×10^{-1}	1.7×10^{-1}
	F	1.1×10^{-4}	3.1×10^{-6}	1.5×10^{-1}	1.1×10^{-2}
Ratio (Evening/Morning)	Lower E	0.82			
	Upper E	0.91			
	F	2.5			

(b)

MLT	Layer	α or β value	α or β 95% confidence	γ value	γ 95% confidence
Evening	Lower E	1.3×10^{-1}	9.0×10^{-3}	-9.2×10^{-1}	2.3×10^{-1}
	Upper E	1.0×10^{-1}	3.6×10^{-3}	-6.6×10^{-1}	1.5×10^{-1}
	F	5.1×10^{-6}	2.0×10^{-7}	1.2×10^{-3}	1.9×10^{-4}
Morning	Lower E	1.8×10^{-1}	4.3×10^{-3}	-1.7	1.9×10^{-1}
	Upper E	9.4×10^{-2}	2.1×10^{-3}	-1.1×10^{-1}	1.5×10^{-1}
	F	2.9×10^{-6}	8.8×10^{-8}	2.6×10^{-3}	3.1×10^{-4}
Ratio (Evening/Morning)	Lower E	0.72			
	Upper E	1.1			
	F	1.8			

ionization in the D region, whereas the Pedersen conductivity tends to peak around 120 km where the ion-neutral collision frequency is equal to the ion gyrofrequency (Schlegel, 1988). Figure 3 shows that the upper E region contributes more than 80 % of the total of the Pedersen conductance and that the lower and the upper E regions contribute equally to the Hall conductance. On the other hand, the bottom side of the auroral emission layers for 427.8 nm and 557.7 nm has a sharp edge (*e.g.*, Semeter *et al*., 2001). This means that these emission intensities may be smaller during a D region ionization event than during an E region event, although the Hall conductance can be larger during D region ionization than during E region ionization. Thus, coefficients of the Hall conductance in the lower E region
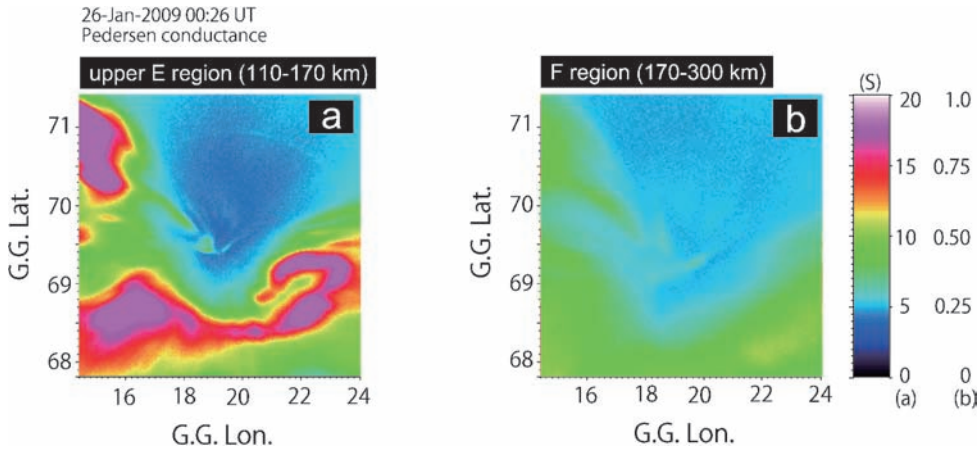
Fig. 6. An example of the horizontal patterns of the Pedersen conductance in (a) the upper E *region (110–170 km) and (b) the* F *region (170–300 km), derived from the 557.7 nm and 630.0 nm emission intensities, respectively, and measured with the all-sky camera at Tromsø. The best-fitted coefficients presented in Table 2 were applied to make this figure.*

may depend on the MLT.

   To assess the validity of this hypothesis, the best-fitted coefficients are tabulated in Tables 7 a and b and the data are classified into two time intervals: magnetic pre-midnight, or evening, and magnetic post-midnight, or morning (the magnetic midnight at Tromsø is approximately 2030 UT). We focus on α in the upper E region for the Pedersen conductance and in the lower and upper E regions for the Hall conductance (hatched gray in Tables 7 a and b) because these three regions are the major portions of each conductance. The ratios of α in the three regions are 0.91, 0.72, and 1.1, respectively. The biggest deviation from unity is for the case of the Hall conductance in the lower E region (*i.e.*, $1.0 - 0.72 = 0.28$). This result is consistent with the hypothesis mentioned above: harder particle precipitation tends to occur more frequently in the morning sector than in the evening sector.

5.3. Example of application to all-sky camera images

   This section derives the horizontal pattern of the conductance by applying the developed method to image data from an all-sky camera. The two-dimensional pattern is useful for various studies, such as those of the ionospheric horizontal current, the field-aligned current (FAC), the Joule and particle heating rate, and the momentum transfer rate via ion drag (Kosch *et al*., 1998, 2000, 2001). This section presents an initial result of the horizontal pattern of the conductance using data from the all-sky camera at the Tromsø EISCAT radar site. The all-sky camera has optical filters of 557.7 nm and 630.0 nm, but no filter of 427.8 nm. The Pedersen conductance may be better than the Hall conductance for test purposes because a portion of the conductance is in the F region. Figure 6 shows horizontal patterns of the Pedersen conductance in (a) the upper E region (110−170 km) and (b) the F region (170−300 km). To make these panels, the three-wavelength method was applied to the 557.7 nm and 630.0 nm data for regions (a) and (b), respectively, with the coefficients summarized in Table 2. The all-sky camera data were taken at 0026 UT on

26 Jan. 2009, when an aurora breakup was occurring. The conductance pattern is mapped in geographic coordinates. As expected, the horizontal pattern at the aurora breakup is complex. The upper E region conductance seems to have finer structures than that for the F region. Auroral particle precipitation causes enhancements of the conductance in the upper E region in association with the upward FAC. The center of image (a) has a dark area, caused by enhancements of recombination and/or evacuation of the ionospheric electrons along the magnetic field line in association with the downward FAC.

6.   Summary and conclusions

EISCAT conductance and auroral emission intensity were compared in order to establish a model function for estimating conductance using photometer data alone. An advantage of the present approach is that allows for derivation of layered conductance. The quality of conductance estimated by the three-wavelength method is the same as that obtained by the one-wavelength method. The layered conductance can be applied to estimate height-dependent parameters, such as the Joule heating rate and effects of ion drag.

Since there is no auroral emission line that always covers the entire ionosphere from 95 to 300 km, we speculated that the one-wavelength method might cause some ambiguities. However, the three-wavelength method did not significantly improve the quality of photometer conductance estimation. Statistics of the particle number flux derived with the CARD method suggest that the emission intensities at 557.7 nm and 427.8 nm may be correlated, and thus either of the wavelengths can represent the entire ionosphere.

Appendix A:
The model function for different border altitudes between the lower and upper *E* region.

Table A. (1) Coefficients of the best-fitted function for the Pedersen conductance. The border altitude between the lower and upper E *regions is presented in the first column from the left. The border altitude between the upper* E *region and the* F *region is 170 km.*
(2) Same as Table A1 but for the Hall conductance.

(1)

Border	Layer	α or β		γ	
		value	95% confidence	value	95% confidence
105 km	Lower *E*	6.8×10^{-3}	1.2×10^{-4}	-9.0×10^{-2}	4.4×10^{-3}
	Upper *E*	1.2×10^{-1}	1.8×10^{-3}	-3.6×10^{-1}	1.1×10^{-1}
110 km	Lower *E*	1.2×10^{-2}	3.3×10^{-4}	-6.1×10^{-2}	1.2×10^{-2}
	Upper *E*	1.1×10^{-1}	1.7×10^{-3}	-2.1×10^{-1}	1.0×10^{-1}
120 km	Lower *E*	6.2×10^{-2}	1.2×10^{-3}	-5.4×10^{-1}	4.5×10^{-2}
	Upper *E*	8.6×10^{-2}	1.5×10^{-3}	-1.2×10^{-1}	8.6×10^{-2}
	F	1.1×10^{-4}	3.1×10^{-6}	1.6×10^{-1}	8.3×10^{-3}

(2)

Border	Layer	α or β		γ	
		value	95% confidence	value	95% confidence
105 km	Lower *E*	1.4×10^{-1}	2.6×10^{-3}	-1.9	9.6×10^{-2}
	Upper *E*	1.7×10^{-1}	2.6×10^{-3}	-1.1	1.5×10^{-1}
110 km	Lower *E*	1.8×10^{-1}	3.6×10^{-3}	-1.9	1.3×10^{-1}
	Upper *E*	9.6×10^{-2}	1.6×10^{-3}	-2.9×10^{-1}	9.7×10^{-2}
120 km	Lower *E*	3.5×10^{-1}	5.9×10^{-3}	-3.7	2.2×10^{-1}
	Upper *E*	4.6×10^{-2}	7.7×10^{-4}	1.1×10^{-1}	4.5×10^{-2}
	F	3.0×10^{-6}	7.1×10^{-8}	2.4×10^{-3}	1.9×10^{-4}

Acknowledgements

References

Ahn, B.-H., Robinson, R.M., Kamide, Y. and Akasofu, S.-I. (1983): Electric conductivities, electric fields and

auroral particle energy injection rate in the auroral ionosphere and their empirical relations to the horizontal magnetic disturbances. Planet. Space Sci., **31**, 641–653, doi: 10.1016/0032–0633(83)90005–3.

Ansari, Z.A. (1964): The aurorally associated absorption of cosmic noise at College, Alaska. J. Geophys. Res., **69**, 4493–4513, doi: 10.1029/JZ069i021p04493.

Banks, P.M., Foster, J.C. and Doupnik, J.R. (1981): Chatanika Radar observations relating to the latitudinal and local time variations of Joule heating. J. Geophys. Res., **86**, 6869–6878, doi: 10.1029/JA086iA08p06869.

Brekke, A. and Hall, C. (1988): Auroral ionospheric quiet summer time conductances. Ann. Geophys., **6**, 361–376.

Brekke, A. and Moen, J. (1993): Observations of high latitude ionospheric conductances. J. Atmos. Terr. Phys., **55**, 1493–1512, doi: 10.1016/0021–9169(93)90126-J.

Brekke, A., Doupnik, J.R. and Banks, P.M. (1974): Incoherent scatter measurements of *E* region conductivities and currents in the auroral zone. J. Geophys. Res., **79**, 3773–3790, doi: 10.1029/JA079i025p03773.

Brekke, A., Hall, C. and Hansen, T.L. (1989): Auroral ionospheric conductances during disturbed conditions. Ann. Geophys., **7**, 269–280.

Campbell, W.H. and Leinbach, H. (1961): Ionospheric absorption at times of auroral and magnetic pulsations. J. Geophys. Res., **66**, 25–34, doi: 10.1029/JZ066i001p00025.

Fujii, R. *et al.* (1995): Comparison between electron spectra calculated from EISCAT electron density profiles and those observed by the DMSP satellites. J. Geomagn. Geoelectr., **47**, 771–782, doi: 10.5636/jgg.47.771.

Gustavsson, B. *et al.* (2000): First tomographic estimate of volume distribution of HF-pump enhanced airglow emission. J. Geophys. Res., **106**, 29105–29123, doi: 10.1029/2000JA900167.

Hardy, D.A. and Gussenhoven, M.S. (1985): A statistical model of auroral electron precipitation. J. Geophys. Res., **90**, 4229–4248, doi: 10.1029/JA090iA05p04229.

Kosch, M.J., Hagfors, T. and Schlegel, K. (1998): Extrapolating EISCAT Pedersen conductances to other parts of the sky using ground-based TV auroral images. Ann. Geophys., **16**, 583–588, doi: 10.1007/s00585–998–0583-y.

Kosch, M.J., Amm, O. and Scourfield, M.W.J. (2000): A plasma vortex revisited: The importance of including ionospheric conductivity measurements. J. Geophys. Res., **105**, 24889–24898, doi: 10.1029/2000JA900102.

Kosch, M.J., Honary, F., del Pozo, C.F., Marple, S.R. and Hagfors, T. (2001): High-resolution maps of the characteristic energy of precipitating auroral particles. J. Geophys. Res., **106**, 28925–28937, doi: 10.1029/2001JA900107.

Mende, S.B., Eather, R.H., Rees, M.H., Vondrak, R.R. and Robinson, R.M. (1984): Optical mapping of ionospheric conductance. J. Geophys. Res., **89**, 1755–1763, doi: 10.1029/JA089iA03p01755.

Moen, J. and Brekke, A. (1993): The solar flux influence on quiet time conductances in the auroral ionosphere. Geophys. Res. Lett., **20**, 971–974, doi: 10.1029/92GL02109.

Oyama, S. *et al.* (2000): Effects of atmospheric oscillations on the field-aligned ion motions in the polar *F*-region. Ann. Geophys., **18**, 1154–1163, doi: 10.1007/s00585–000–1154-z.

Rasmussen, C.E. and Schunk, R.W. (1988): A photochemical equilibrium model for ionospheric conductivity. J. Geophys. Res., **93**, 9831–9840, doi: 10.1029/JA093iA09p09831.

Robinson, R.M. and Vondrak, R.R. (1984): Measurements of *E* region ionization and conductivity produced by solar illumination at high latitudes. J. Geophys. Res., **89**, 3951–3956, doi: 10.1029/JA089 iA06 p03951.

Robinson, R.M., Vondrak, R.R. and Potemra, T.A. (1985): Auroral zone conductivities within the field-aligned current sheets. J. Geophys. Res., **90**, 9688–9696, doi: 10.1029/JA090iA10p09688.

Robinson, R.M., Vondrak, R.R., Miller, K., Dabbs, T. and Hardy, D. (1987): On calculating ionospheric conductances from the flux and energy of precipitating electrons. J. Geophys. Res., **92**, 2565–2569, doi: 10.1029/JA092iA03p02565.

Robinson, R.M., Vondrak, R.R., Craven, J.D., Frank, L.A. and Miller, K. (1989): A comparison of ionospheric conductances and auroral luminosities observed simultaneously with the Chatanika Radar and the DE 1 auroral imagers. J. Geophys. Res., **94**, 5382–5396, doi: 10.1029/JA094iA05p05382.

Schlegel, K. (1988): Auroral zone *E*-region conductivities during solar minimum derived from EISCAT data. Ann. Geophys., **6**, 129–138.

Schuster, A. (1908): The diurnal variation of terrestrial magnetism. Philos. T. R. Soc. Lond., **208**, 163–204.

Schuster, A. and Lamb H. (1889): The diurnal variation of terrestrial magnetism. Philos. T. R. Soc. Lond., **180**, 467–518.

Semeter, J., Lummerzheim, D. and Haerendel, G. (2001): Simultaneous multispectral imaging of the discrete aurora. J. Atmos. Sol.-Terr. Phy., **63**, 1981–1992, doi: 10.1016/S1364–6826(01)00074–8.

Senior, A., Kavanagh, A.J., Kosch, M.J. and Honary, F. (2007): Statistical relationships between cosmic radio noise absorption and ionospheric electrical conductances in the auroral zone. J. Geophys. Res., **112**, A11301, doi: 10.1029/2007JA012519.

Senior, C. (1991): Solar and particle contributions to auroral height-integrated conductivities from EISCAT data: a statistical study. Ann. Geophys., **9**, 449–460.

Vickrey, J.F., Vondrak, R.R. and Matthews, S.J. (1981): The diurnal and latitudinal variation of auroral zone ionospheric conductivity. J. Geophys. Res., **86**, 65–75, doi: 10.1029/JA086iA01p00065.

Vickrey, J.F., Vondrak, R.R. and Matthews, S.J. (1982): Energy deposition by precipitating particles and Joule dissipation in the auroral ionosphere. J. Geophys. Res., **87**, 5184–5196, doi: 10.1029/JA087iA07p05184.

Vondrak, R.R. and Baron, M.J. (1976): Radar measurements of the latitudinal variation of auroral ionization. Radio Sci., **11**, 939–946, doi: 10.1029/RS011i011p00939.

Vondrak, R. and Robinson, R. (1985): Inference of high-latitude ionization and conductivity from AE-C measurements of auroral electron fluxes. J. Geophys. Res., **90**, 7505–7512, doi: 10.1029/JA090iA08p07505.

Walker, J.K. and Bhatnagar, V.P. (1989): Ionospheric absorption, typical ionization, conductivity, and possible synoptic heating parameters in the upper atmosphere. J. Geophys. Res., **94**, 3713–3720, doi: 10.1029/JA094iA04p03713.

Wallis, D.D. and Budzinski, E.E. (1981): Empirical models of height integrated conductivities. J. Geophys. Res., **86**, 125–137, doi: 10.1029/JA086iA01p00125.